Available online at www.sciencedirect.com
ScienceDirect
Green Energy & Environment xxx (xxxx) xxx
www.keaipublishing.com/gee

Research paper

Confining MoS_2 nanocrystals in MOF-derived carbon for high performance lithium and potassium storage

Chen Hu [a], Kun Ma [a], Yanjie Hu [a], Aiping Chen [a,**], Petr Saha [b], Hao Jiang [a,*], Chunzhong Li [a]

[a] Key Laboratory for Ultrafine Materials of Ministry of Education, Shanghai Engineering Research Center of Hierarchical Nanomaterials, School of Materials Science and Engineering, East China University of Science & Technology, Shanghai, 200237, China
[b] Centre of Polymer Systems, University Institute, Tomas Bata University in Zlin, Trida T. Bati 5678, 760 01, Zlin, Czech Republic

Received 9 November 2019; revised 30 December 2019; accepted 3 February 2020
Available online ■ ■ ■

Abstract

Developing an efficient synthesis protocol to simultaneously control 2D nanomaterials' size and dispersion is the pivot to optimize their electrochemical performance. Herein, we report the synthesis of uniform MoS_2 nanocrystals well-anchored into the void space of porous carbon (donated as $MoS_2 \subset C$ hybrids) by a simple confined reaction in metal–organic framework (MOF) during carbonization process. The strong confinement effect refrain MoS_2 growth and aggregation, generating abundant active centers and edges, which contribute fast lithium/potassium reaction kinetics. In addition to the hybridization with the derived carbon, the $MoS_2 \subset C$ hybrids exhibit rapid Li^+ transfer rate (~10^{-9} cm^2 s^{-1}) and greatly improved electronic conductivity. Consequently, the $MoS_2 \subset C$ hybrids show ultrafast rate performances and satisfactory cycling stabilities as anode materials for both lithium and potassium ion batteries. This work demonstrates a universal tactic to achieve high dispersive 2D nanomaterials with tailorable particle size.

Keywords: Confined reaction; MoS_2; Nanocrystals; Metal–organic framework; Energy storage

1. Introduction

Two-dimensional (2D) materials have received widespread attention in energy storage fields, such as supercapacitors [1–3] and alkali metal ion batteries [4,5], on account of their unique atomic layer thickness and ultra-large specific surface area [6–11]. Among them, 2D transition metal sulfides (*e.g.* MoS_2) usually deliver a higher actual specific capacity than the theoretical value in lithium-ion batteries (LIBs) [12–14]. This is because the rich edges and the reversible reaction of Li_2S can contribute plentiful additional capacity, which is different from the corresponding metal oxides [15]. Besides that, it is demonstrated that MoS_2 is a burgeoning anode candidate for potassium-ion batteries (KIBs) due to the large interlayer distance, providing ideal spaces for effective K^+ insertion and extraction. Nevertheless, they also suffer from the same drawbacks as metal oxides, such as low conductivity and ions diffusion kinetics, conspicuous volume change and structural pulverization in the continuous charge/discharge process. Meantime, the easy-stacking and sulfur dissolution also affect the storage capacity and cycling stability [16,17].

It is well-accepted that the few-layer MoS_2 nanocrystals can efficaciously mitigate structural stress change and shorten electrons/ions transfer distance, giving impetus to improve the structure stability and lithium/potassium reaction kinetics [18,19]. Meanwhile, more active edges and surfaces have been created, which is critical for alkali metal ions storage because the edges have stronger metal ions binding energy according to the quantum density functional theory (QDFT) calculations

* Corresponding author.
** Corresponding author.
E-mail addresses: apchen@ecust.edu.cn (A. Chen), jianghao@ecust.edu.cn (H. Jiang).

https://doi.org/10.1016/j.gee.2020.02.001

[20,21]. However, the MoS_2 nanocrystals is prone to aggregation into bigger particles and non-redispersion. The MoS_2/C incorporated nanostructure has been recognized as an effective method to address the above issues, mainly involving the thermal decomposition of the two precursors [22,23]. The matching relationship of the two involved reaction rates have been proved to be very difficult to control, directly influencing the particle size and distribution [24,25]. Therefore, it is critical to exploit a simple and general strategy to controllably synthesize such incorporated nanostructures.

Metal–organic frameworks (MOFs) have attracted great attention in the adsorption and separation fields in view of its plentiful pores [26–29], which can be applied as confinement space to anchor and disperse targeted compounds. Inspired by this concept, we realize the confinement of few-layer MoS_2 nanocrystals (<10 nm) into MOF-derived porous carbon ($MoS_2 \subset C$) by choosing a stable chromium-based MOF (MIL-101). The as-prepared $MoS_2 \subset C$ hybrids deliver high rate capabilities and long cycling life as LIB and KIB anodes. The excellent electrochemical performance is dominantly ascribed to the smart structure design with rapid electron and ion transfer caused by the strong confinement effect. The present work provides a general synthesis tactic to achieve high dispersive 2D nanomaterials with tailorable particle size.

2. Experimental section

2.1. Synthesis of the $MoS_2 \subset C$ hybrids

In a typical process, MIL-101(Cr) was firstly synthesized *via* the method developed by G. Férey et al. [30] Then, 0.156 g of MIL-101(Cr) was ultrasonically added into 10 mL dimethyl formamide (DMF) solution that contained 0.2 g of ammonium thiomolybdate ($(NH_4)_2MoS_4$). After collecting and drying, the brown precipitates were annealed at 600 °C for 2 h under Ar atmosphere and then etched with mixed solution of dilute sulfuric acid and potassium bromate to remove chromic oxides. Finally, the $MoS_2 \subset C$ hybrids were obtained by washing with deionized water and drying at 80 °C in a vacuum oven. As a control, the ultrasmall MoS_2 nanosheets were also grown on the surface of MIL-101(Cr) derived porous carbon (labelled as MoS_2/C hybrids). In this process, the above mixed solution was directly transferred into 50 mL Teflon-lined stainless steel autoclave and maintained at 210 °C for 24 h, and subsequently through the same carbonization and etching treatment as the $MoS_2 \subset C$ hybrids. The pure MoS_2 sample was prepared by directly annealing $(NH_4)_2MoS_4$ at the same condition.

2.2. Characterization

The morphology and microstructure of the samples were analysed by X-ray power diffract-meter (XRD, Rigaku D/Max2550, Cu Kα radiation), scanning electron microscopy (SEM, Hitachi, S-4800) with an X-ray energy dispersive spectrometer (EDS), transmission electron microscopy (TEM, JEOL-2100F) and scanning transmission electron microscopy (STEM, FEI Tecnai G2 F20). Raman spectra were tested by NEXUS 670 FT-IR & Raman spectrometer. Nitrogen adsorption–desorption isotherms were determined by Brunauer–Emmett–Teller (BET) measurement using a Micromeritics ASAP 2020 surface area analyzer. The MoS_2 content was obtained by thermogravimetric analysis (NETZSCH STA409PC) test with a heating rate of 10 °C min^{-1} under flowing air. The X-ray photoelectron spectroscopy (XPS) was recorded with AXIS Ultra DLD spectrometer (Al Kα X-ray source).

2.3. Electrochemical measurements

Electrochemical measurements were performed using 2032 coin-type cells. The working electrode was obtained by mixing 80 wt% active materials, 10 wt% carbon Super P, and 10 wt% poly(vinylidene difluoride) (PVDF) and then coating them on a copper foil by a doctor blade. As for LIBs, the counter electrode and separator were pure lithium foil and polypropylene membrane (Celgard 2400). The electrolyte was 1 M lithium hexafluorophosphate ($LiPF_6$) in ethylene carbonate (EC) and diemethyl carbonate (DMC) (volume ratio = 1:1). For the KIBs, the counter electrode and separator were pure potassium foil and Whatman GF/D. And the electrolyte was 0.8 M potassium hexafluorophosphate (KPF_6) in EC and DMC (volume ratio = 1:1). The charge–discharge measurements were carried out on a LAND-CT2001C test system. Cyclic voltammogram experiment was performed from 0.01 to 3V on an Autolab PGSTAT302N electrochemical workstation. The impedance spectra were measured on constant voltage mode with the frequency range from 100 kHz to 0.01 Hz.

3. Results and discussion

Fig. 1a schematically illustrates the fabrication process of the $MoS_2 \subset C$ hybrids. The MIL-101(Cr) MOF with a typical octahedral morphology has been chosen as confined space because of its high Brunauer–Emmett–Teller (BET) surface area of 2313 m^2 g^{-1} and two large cavities of 2.9 and 3.4 nm (Fig. S1). After absorbing the $(NH_4)_2MoS_4$ dispersed solution and the subsequent carbonization, the MoS_2 nanocrystals can be harvested and confined into MOF-derived porous carbon. The residual chromic oxides can be completely removed by dilute sulfuric acid and potassium bromate etching, which has been verified by the EDS and XPS results of the products before and after etching (Fig. S2). As shown in Fig. 1b, the $MoS_2 \subset C$ hybrids also show well-maintained nano-octahedron with high uniformity and the average edge length is about 150 nm, where no obvious MoS_2 nanosheets are observed on the surface. Fig. 1c provides the transmission electron microscopy (TEM) observation of the $MoS_2 \subset C$ hybrids, the numerous 1–3 layered MoS_2 nanocrystals with sizes of <10 nm are homogenously incorporated into the MOF-derived carbon skeletons. And the (002) plane interlayer spacing of few-layer MoS_2 nanocrystals is 0.67 nm. The selected-area electron diffraction (SAED) pattern (inset of Fig. 1c) reveals the 2H phase MoS_2 without any other impurity. The further elemental distributions of the $MoS_2 \subset C$ hybrids are shown in

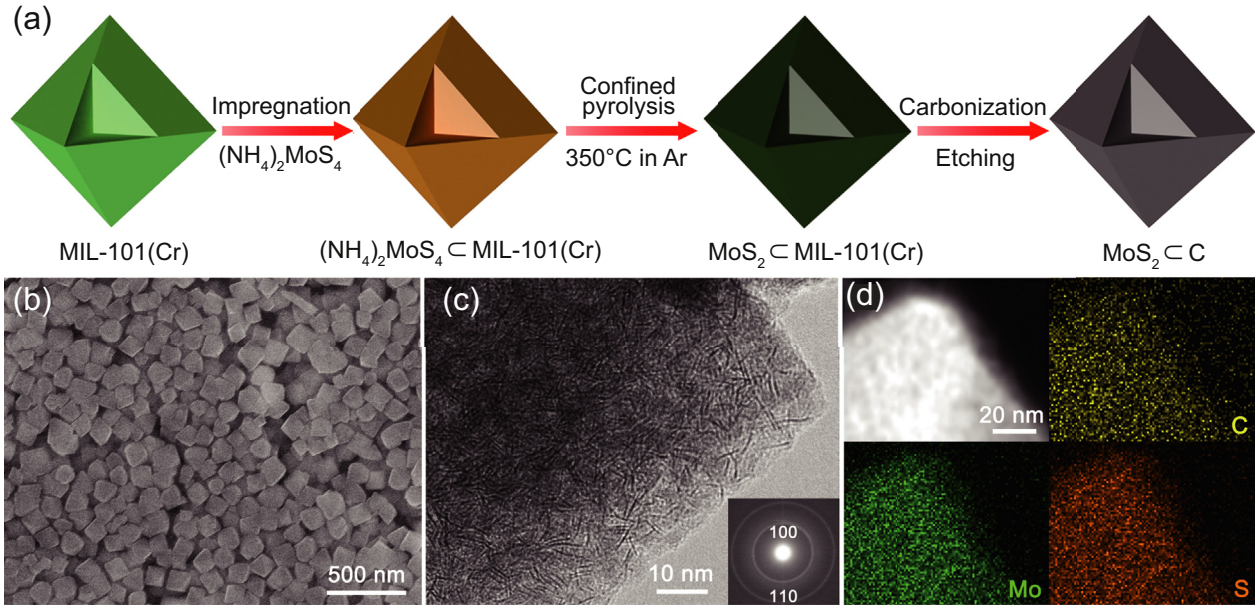

Fig. 1. (a) Schematic illustration of the fabrication process, (b) SEM image, (c) high-resolution TEM image and (d) STEM-EDS mapping of the as-synthesized $MoS_2 \subset C$ hybrids (inset of (c) showing the corresponding SAED pattern).

Fig. 1d. It can be observed that all of Mo and S elements uniformly distribute in the carbon matrix. To highlight the confinement effect, the MoS_2/C hybrids are also synthesized as a control by a simple hydrothermal route, in which few-layer MoS_2 nanosheets have been grown on the surface of MOF-derived carbon (Fig. S3).

To investigate the formation mechanism of the MoS_2 nanocrystals in the MOF-confined space, the thermogravimetric (TG) analyses of $(NH_4)_2MoS_4$, MIL-101(Cr) and $(NH_4)_2MoS_4 \subset$MIL-101(Cr) have been performed in Fig. S4a. The corresponding TEM observations and schematic illustrations are further provided in Fig. 2. Before 210 °C, the $(NH_4)_2MoS_4$ is decomposed into amorphous MoS_3 and MoS_2 with the releasing of NH_3, H_2S and partial sulfur, which results in 38% mass ratio loss. Fig. 2a and d indicate no crystal lattice can be found in the cavities of MIL-101(Cr) at 210 °C, further supporting above analysis. When the temperature increases from 350 °C to 450 °C, another 10% mass loss can be observed owing to the residual sulfur evaporation and MIL-101(Cr) carbonization accompanied with the generation of pure MoS_2 crystals. The TEM image of products at 350 °C is exhibited in Fig. 2b and e, non-carbonized MIL-101(Cr) maintains its original structure where 1–3 layered MoS_2 nanocrystal with a size of less than 3 nm can be observed. This fact indicates the nanocages inhibit the excessive agglomeration and growth during grain formation stage. The hybrids are further annealed at 600 °C to stabilize the structure and improve the conductivity (Fig. 2c and f). The shape of

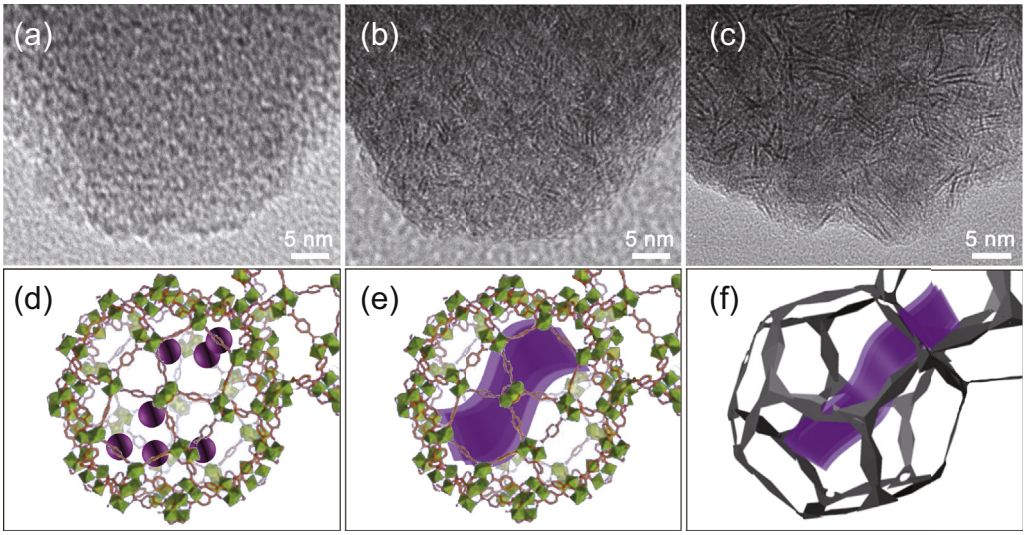

Fig. 2. TEM images and schematic illustrations of the $(NH_4)_2MoS_4 \subset$MIL-101(Cr) annealed in Ar atmosphere at (a, d) 210 °C (b, e) 350 °C, and (c, f) 600 °C.

carbonized MOF shows slight changes and the lengths of MoS_2 crystals increase to about 10 nm. Notably, the layer numbers of MoS_2 can keep within three, implying that the MoS_2 nanocrystals are separated by carbon. The corresponding differential thermogravimetric (DTG) curves further verify the above analysis (Fig. S4b). Interestingly, the mass loss peaks (1# and 2#) of $(NH_4)_2MoS_4$ shift to lower temperatures in $(NH_4)_2MoS_4 \subset$MIL-101(Cr), which may be due to the tendency of the molecules in nanocages to bond with each other, giving driving force for pyrolysis. Based on the above results, the formation mechanism can be separated into three stages: amorphous molybdenum sulfides$\subset$MIL-101(Cr) at 210 °C, MoS_2 crystals$\subset$MIL-101(Cr) at 350 °C and MoS_2 crystals$\subset$carbonized MIL-101(Cr) at 600 °C. Such process analysis directs the synthesis of the $MoS_2 \subset$C hybrids and confirms that uniform ultrasmall 2D nanocrystals can be easily achieved by the unique MOF-confined synthesis tactic.

The crystalline structure of the $MoS_2 \subset$C hybrids and the MoS_2/C hybrids are characterized by X-ray diffraction (XRD), as shown in Fig. 3a. All the diffraction peaks can be indexed to the 2H phase MoS_2 (JCPDS: 37–1492), which are in accordance with the SAED pattern. Compared with the MoS_2/C hybrids, the MoS_2 (002) peak in the $MoS_2 \subset$C hybrids becomes very weak with a shift to small angle, suggesting the formation of few-layer MoS_2 nanocrystals with an enlarged interlayer distance. It is well-accepted that the peak separation (Δk) between the in-plane Mo–S mode (E^1_{2g}) and out-of-plane Mo–S mode (A_{1g}) in the Raman spectra is related to the layer numbers of MoS_2 [31–33]. Fig. 3b shows the $MoS_2 \subset$C hybrids give a Δk value of 22.1 cm^{-1} (close to 20.2–21.2 cm^{-1} for monolayer MoS_2), which is much lower than the MoS_2/C hybrids (23.2 cm^{-1}) and the pure MoS_2 (26.1 cm^{-1}). The BET surface area of $MoS_2 \subset$C hybrids is measured to be 118.5 $m^2\ g^{-1}$ (Fig. 3c). After removing the MoS_2 nanocrystals by hot concentrated nitric acid, the resultant porous carbon framework shows a significantly increased BET surface area of 330.5 $m^2\ g^{-1}$ with a typical mesoporous characteristic. The corresponding TEM image provides a direct evidence in the inset of Fig. 3c. A new pore size distribution centred at 15.4 nm can be observed for the porous carbon in Fig. S5. The above results totally verify the successful confinement of few-layer MoS_2 nanocrystals into MOF-derived carbon frameworks. The MoS_2 content in the $MoS_2 \subset$C hybrids is about 48.9% according to TG results (Fig. S6). The X-ray photoelectron spectroscopy (XPS) is employed to understand the electronic structure of the product. Fig. 3d gives high resolution Mo 3d spectra of the $MoS_2 \subset$C and the MoS_2/C. Two main Mo^{4+} characteristic peaks at 229.2 eV and 232.5 eV represent Mo $3d_{5/2}$ and Mo $3d_{3/2}$ of the Mo–S bond, respectively [34]. It is noted that a pair of small peaks at 228.8/231.8 eV corresponding to Mo–C bond [35], appears in the $MoS_2 \subset$C hybrids while cannot be found in MoS_2/C hybrids. The emergence of Mo–C bond indicates the strong interaction between MoS_2 and porous carbon frameworks, which is beneficial for enhancing the structural stability.

All the products are assembled into the 2032 coin-type half cells to evaluate their electrochemical performances. Fig. 4a provides the initial three cyclic voltammetry (CV) curves of the $MoS_2 \subset$C hybrids in the potential range of 0.01–3.0 V at 0.2 mV s^{-1}. The peaks at 1.15 V and 0.58 V in the first

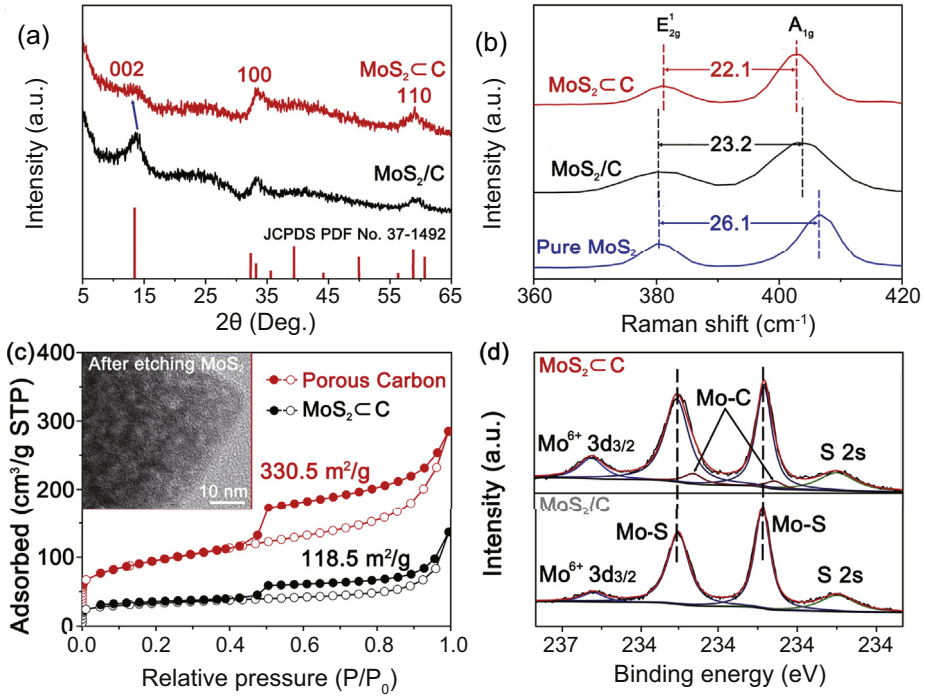

Fig. 3. (a) XRD patterns of the $MoS_2 \subset$C hybrids and the MoS_2/C hybrids, (b) Raman spectra of the $MoS_2 \subset$C hybrids, the MoS_2/C hybrids and the pure MoS_2, (c) N_2 adsorption–desorption isotherms of the $MoS_2 \subset$C hybrids and the corresponding porous carbon after etching MoS_2 (inset showing the TEM image of porous carbon), and (d) high-resolution Mo 3d spectra of the $MoS_2 \subset$C hybrids and the MoS_2/C hybrids.

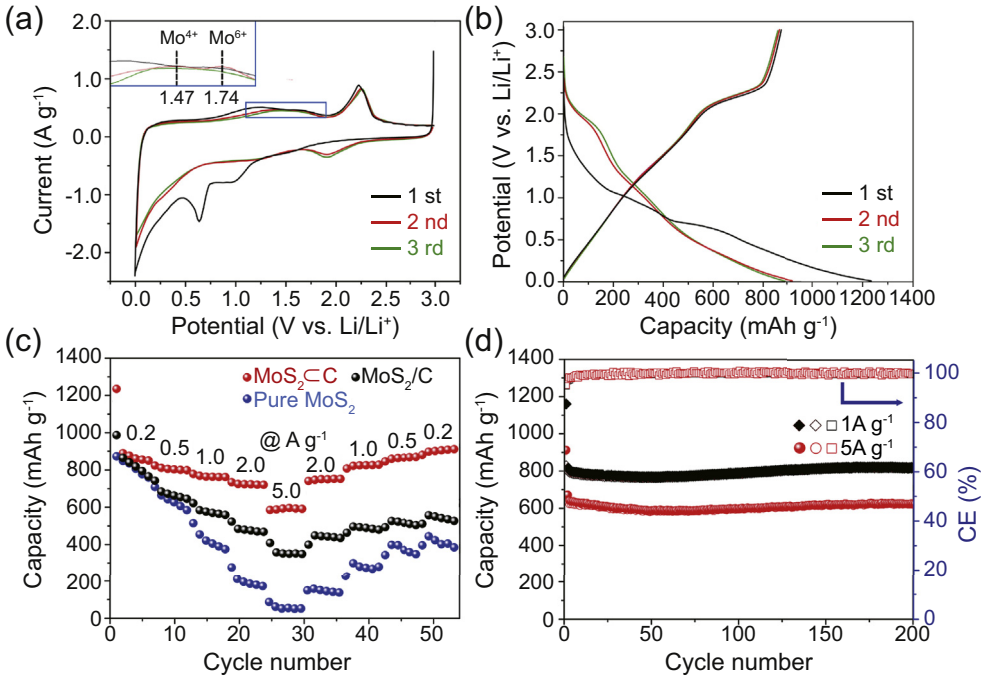

Fig. 4. Electrochemical performance for LIBs. (a) The initial three CV curves at 0.2 mV s^{-1} and (b) charge–discharge curves at 0.2 A g^{-1} of the MoS_2⊂C hybrids, (c) rate capabilities of the MoS_2⊂C hybrids, the MoS_2/C hybrids and the pure MoS_2, and (d) cycling performances of the MoS_2⊂C hybrids at 1.0 and 5.0 A g^{-1} for 200 cycles.

cathodic scan belong to the intercalation and conversion reaction to form Li_xMoS_2 and Li_2S/Mo, respectively [36]. In the anodic scans, two reversible oxidation peaks of Mo to Mo^{4+} and Mo^{6+} are detected at 1.47 V and 1.74 V [37]. It is reported that the electropositive Mo^{4+}/Mo^{6+} possessed a strong affinity for polysulfides, effectively restraining the sulfur dissolution during cycling. The oxidation/reduction peaks around 2.3 V/1.8 V in the subsequent two cycles are attributed to the reversible reaction of S and Li_2S. Fig. 4b shows the galvanostatic charge/discharge curves of the MoS_2⊂C hybrids for

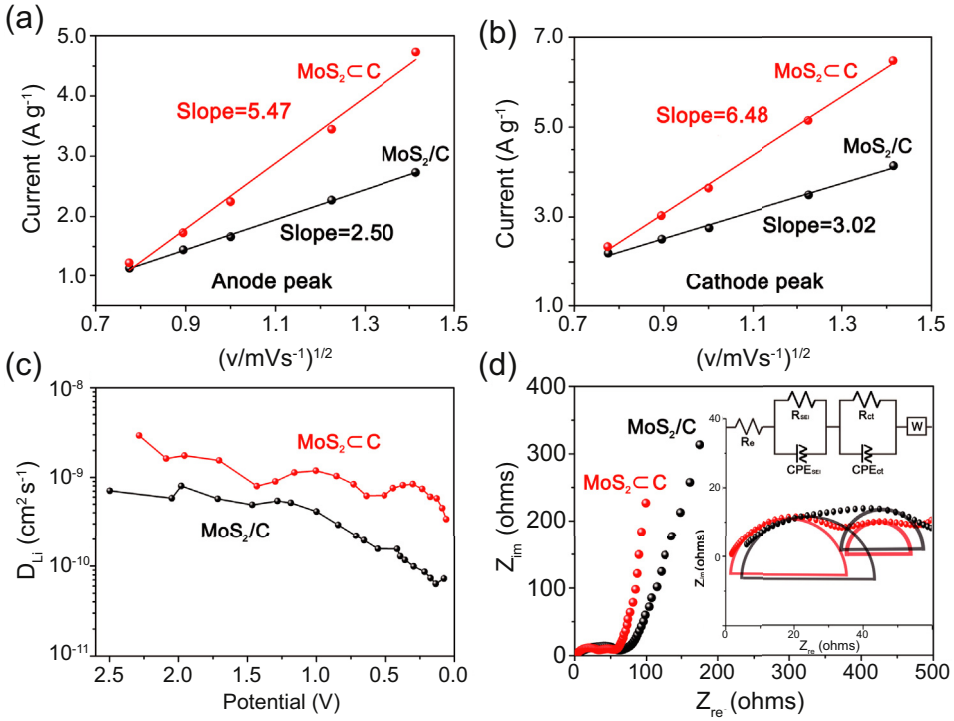

Fig. 5. (a, b) Linear relationship of the anode/cathode peak current (i_p) and the square root of the scan rate ($v^{1/2}$) for the MoS_2⊂C hybrids and the MoS_2/C hybrids, (c) GITT curves and (d) EIS spectra of the MoS_2⊂C hybrids and the MoS_2/C hybrids.

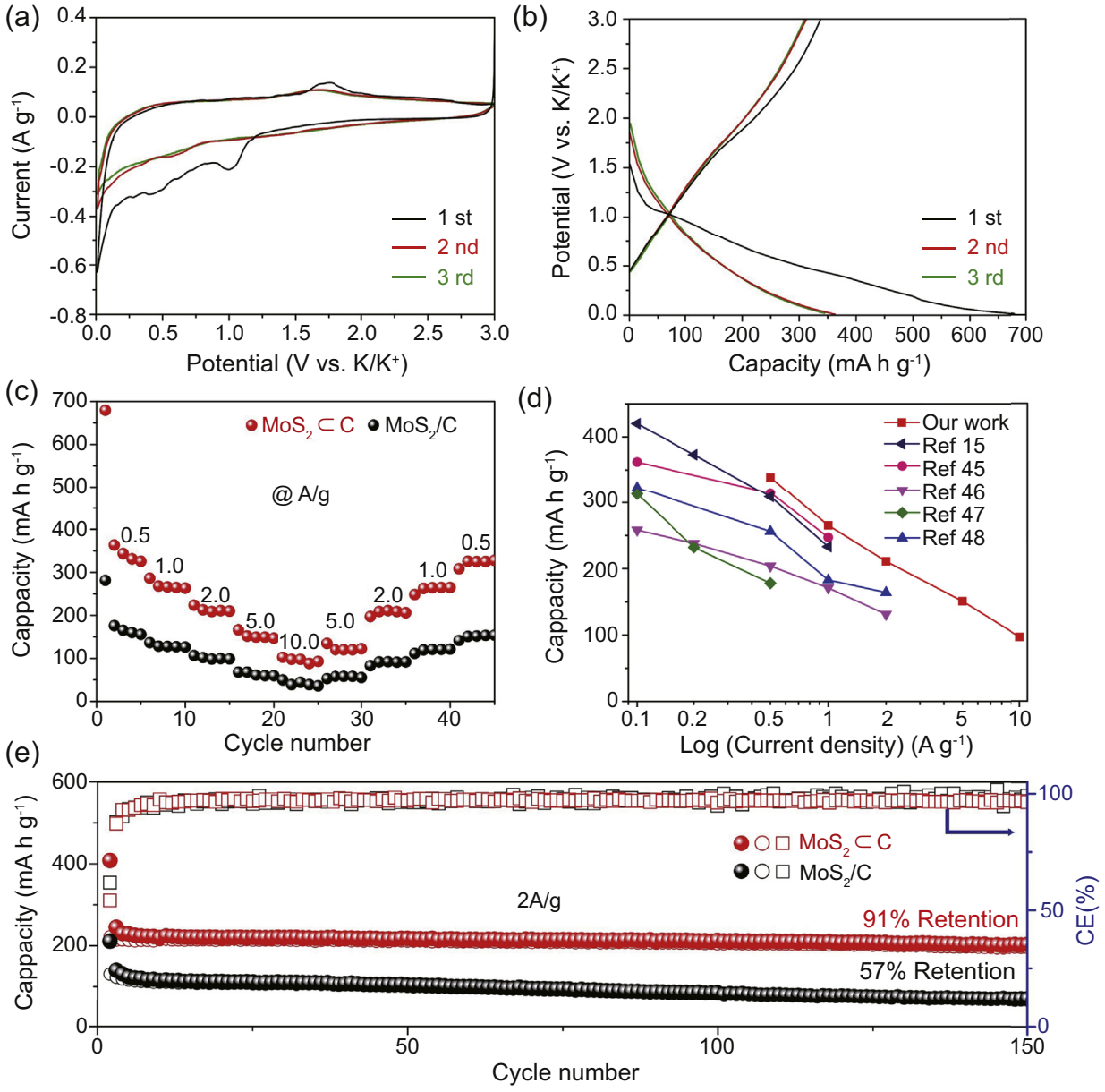

Fig. 6. Electrochemical performance for KIBs. (a) The initial three CV curves at 0.2 mV s^{-1} and (b) charge–discharge curves at 0.5 A g^{-1} of the MoS_2⊂C hybrids, (c) rate capabilities of the MoS_2⊂C hybrids and the MoS_2/C hybrids, (d) the comparison of rate retention of MoS_2 based anode materials for KIBs and (e) capacity retention of the MoS_2⊂C hybrids and the MoS_2/C hybrids at 2.0 A g^{-1} for 150 cycles.

the first three cycles at a current density of 200 mA g^{-1}. And the initial discharge capacity of the MoS_2⊂C hybrids reaches 1233.7 mAh g^{-1} with a Coulombic efficiency (CE) of 70.7%. The capacity irreversibility is due to the formation of SEI film. In addition, the second and third cycling curves are almost overlapped with a near 100% CE. Fig. 4c depicts the rate performance of the MoS_2⊂C hybrids, the average reversible capacities are 870, 803, 764, 722, 592 mAh g^{-1} at current densities of 0.2, 0.5, 1.0, 2.0, 5.0 A g^{-1}, respectively. On the contrary, the MoS_2/C hybrids and the pure MoS_2 exhibit much lower capacities of 360 and 55 mAh g^{-1} at 5.0 A g^{-1} (Fig. S7), respectively. Furthermore, as the current density returning to 0.2 A g^{-1}, because of the structural defects and polysulfide shuttling effect, the MoS_2/C hybrids and the pure MoS_2 show obvious capacity decay. Fig. 4d further gives the cycling stability of the MoS_2⊂C hybrids that no obvious capacity loss can be observed at 1.0 A g^{-1}. And even the current density up to 5.0 A g^{-1}, a specific capacity of 600 mAh g^{-1} with 100% capacity retention is still achieved after 200 cycles. However, the MoS_2/C hybrids shows a rapid capacity fading of 260 mAh g^{-1} at 5 A g^{-1} after 200 cycles (Fig. S8). Such property of stable energy output exceeds many recently reported MoS_2-based materials [38–40]. For example, Wang et al. fabricated the MoS_2/Graphene 2D heterostructures for LIBs, which show high rate performances of 970 mAh g^{-1} at 5A. However, the capacity loss is over 30% in 150 cycles at

1 A g^{-1}, mainly due to the undesired side reactions which are caused by directly exposing MoS_2 in the electrolyte.

In order to well understand the structure advantages, Li^+ diffusion kinetics of the $MoS_2\subset C$ hybrids and the MoS_2/C hybrids are investigated. According to the CV curves at various scan rates (Fig. S9), the relationship of peak current (i_p) and the square root of scan rate ($v^{1/2}$) provided in Fig. 5a&5b and can be interpreted by the Randles–Sevcik equation (Equation (1)) [41,42].

$$i_p = \left(2.69\times10^5\right)n^{3/2}\times S\times D_{Li^+}^{1/2}\times C\times v^{1/2} \quad (1)$$

where i_p is the peak current, n is the number of charge-transfer, S is the area of electrode, C is the concentration of Li^+, and v is the sweep rate. As the values of n, S, and C are constant and equal in both electrodes, the Li^+ diffusion coefficients ($D_{Li}{}^+$) are positively related to the slope of i_p-$v^{1/2}$ curves. The linear curves indicate that the electrodes are diffusion-controlled. Specifically, the larger slopes in both cathodic and anodic scans for the $MoS_2\subset C$ hybrids suggest the rapider ion diffusion rates compared to MoS_2/C hybrids. To further quantify the $D_{Li}{}^+$ throughout the Li^+ insertion process, galvanostatic intermittent titration technique (GITT) study is employed. The cell is discharged at 200 mA g^{-1} for 20 min followed by a relaxation time interval of 120 min, and this procedure is repeated until the voltage reached 0.01 V. The $D_{Li}{}^+$ can be calculated by Equation (2): [43,44].

$$D_{Li^+} = \frac{4}{\pi\tau}\left(\frac{m_B V_M}{M_B A}\right)^2\left(\frac{\Delta E_S}{\Delta E_\tau}\right)^2 \quad (2)$$

where m_B, V_M and M_B are the mass, molar volume, and molecular weight of the active materials, respectively. A is the contact area between the active material and the electrolyte. ΔE_S, ΔE_τ and τ are demonstrated in a typical GITT step at around 1.0 V in Fig. S10. The calculated $D_{Li}{}^+$ values are summarized in Fig. 5c, and the results reveal that the $D_{Li}{}^+$ of the $MoS_2\subset C$ hybrids can reach a high value of 10^{-9} orders of magnitude, which is higher than that of the MoS_2/C hybrids at all voltages. The $D_{Li}{}^+$ shows a downward trend at low-voltage region, which is mainly attributed to the gradually increased Li^+ concentration in active materials, weakening the concentration diffusion effect. The faster ion diffusion ability is also confirmed by electrochemical impedance spectra (EIS) results (Fig. 5d). Besides, the high-frequency region in EIS curves can be fitting by the typical LIBs circuit model, and the details are shown in Fig. S11. The curves can be separated to two semicircles, which are related to SEI resistances (R_{SEI}) and charge-transfer resistances (R_{ct}), as drawn in the inset of Fig. 5d. Specifically, the $MoS_2\subset C$ hybrids exhibit the lower R_{SEI} (34.7 Ω) and R_{ct} (14.0 Ω) compared to MoS_2/C hybrids (39.5 for R_{SEI} and 19.5 Ω for R_{ct}). The rapid electron/ion transfer rates can be attributed to shorten the diffusion length that created by the high edge-density and surface exposure of MoS_2 in the $MoS_2\subset C$ hybrids.

As a promising candidate for next energy storage systems, KIBs have aroused extensive interest in view of the low price and abundant potassium supplies. The potassium storage properties of the $MoS_2\subset C$ electrodes are also investigated. Fig. 6a gives the first three CV cycles of the $MoS_2\subset C$ hybrids for KIBs. The reduction peaks appear at 1.1V and 0.4V is ascribed to the reaction between K^+ and MoS_2 to form K_xMoS_2 and K_xS/Mo, respectively. And the corresponding depotassiation peaks can be found at around 1.7V in the anodic scans. The peak potentials are well consistent with the interlayer-expended MoS_2 in a previous report [44]. The charge/discharge profiles at a current density of 0.5 A g^{-1} are shown in Fig. 6b the discharge and charge capacity are 679 and 337 with an ICE of 49.6%. Furthermore, the $MoS_2\subset C$ hybrids can obtain the average specific capacities of 341, 266 and 211 mA h g^{-1} at 0.5, 1.0, and 2.0 A g^{-1}, respectively. Even at 5.0 and 10.0 A g^{-1}, 149 and 94 mA h g^{-1} are remained, much higher than the MoS_2/C hybrids (Fig. 6c). Such high rate capabilities are not reached in other MoS_2 based anodes (Fig. 6d&Table S1) [45–49]. In addition, the $MoS_2\subset C$ hybrids can also show excellent cycling performance with a 91% capacity retention at 2.0 A g^{-1} after 150 cycles, which is far superior to that of the MoS_2/C hybrids (Fig. 6e).

4. Conclusion

In summary, we demonstrate an effective nanoconfined strategy to incorporate well-dispersed 1–3 layered MoS_2 nanocrystals in MOF derived porous carbon. The highly dispersed MoS_2 nanocrystals with sizes of less than 10 nm expose huge active surfaces/edges. Combining with the benefits of carbonized MOF, the as-designed $MoS_2\subset C$ hybrids show a rapid Li^+ transfer and enhanced electronic conductivity. The features endow $MoS_2\subset C$ hybrids with much better lithium/potassium storage properties than the MoS_2/C hybrids and the corresponding pure MoS_2. Specifically, the $MoS_2\subset C$ hybrids deliver a high specific capacity of 870 mAh g^{-1} at 200 mA g^{-1} with intriguing rate capability (592 mAh g^{-1} at 5 A g^{-1}) in LIBs. More importantly, the $MoS_2\subset C$ hybrids exhibit 149 (94) mA h g^{-1} capacities even at 5.0 (10.0) A g^{-1} for KIBs. The present MOF confined strategy provides a new avenue for controlling the size and dispersibility of 2D nanomaterials.

Conflict of interest

The authors declare no competing financial interest.

Acknowledgements

This work was supported by the National Natural Science Foundation of China (21975074, 91534202 and 91834301), the Basic Research Program of Shanghai (17JC1402300), the Shanghai Scientific and Technological Innovation Project (18JC1410500), the National Program for Support of Top-Notch Young Professionals, and the Fundamental Research Funds for the Central Universities (222201718002).

Appendix A. Supplementary data

Supplementary data to this article can be found online at https://doi.org/10.1016/j.gee.2020.02.001.

References

[1] H. Li, X. Li, J. Liang, Y. Chen, Adv. Energy Mater. (2019) 1803987.
[2] E. Martínez-Periñán, M.P. Down, C. Gibaja, E. Lorenzo, F. Zamora, C.E. Banks, Adv. Energy Mater. 8 (2018) 1702606.
[3] K.S. Kumar, N. Choudhary, Y. Jung, J. Thomas, ACS Energy Lett. 3 (2018) 482–495.
[4] Y. Fang, R. Hu, B. Liu, Y. Zhang, K. Zhu, J. Yan, K. Ye, K. Cheng, G. Wang, D. Cao, J. Mater. Chem. 7 (2019) 5363–5372.
[5] J. Xu, J. Mahmood, Y. Dou, S. Dou, F. Li, L. Dai, J.B. Baek, Adv. Mater. 29 (2017) 1702007.
[6] Y. Sun, Q. Wu, G. Shi, Energy Environ. Sci. 4 (2011) 1113.
[7] X. Wang, T.S. Mathis, K. Li, Z. Lin, L. Vlcek, T. Torita, N.C. Osti, C. Hatter, P. Urbankowski, A. Sarycheva, M. Tyagi, E. Mamontov, P. Simon, Y. Gogotsi, Nat. Energy 4 (2019) 241–248.
[8] K. Hantanasirisakul, Y. Gogotsi, Adv. Mater. 30 (2018) 1804779.
[9] D. Er, J. Li, M. Naguib, Y. Gogotsi, V.B. Shenoy, ACS Appl. Mater. Interfaces 6 (2014) 11173–11179.
[10] C. Zhang, S. Park, O. Ronan, A. Harvey, A. Seral-Ascaso, Z. Lin, N. McEvoy, C. Boland, N. Berner, G. Duesberg, P. Rozier, J. Coleman, V. Nicolosi, Small 13 (2017) 1701677.
[11] Y. Wei, Y. Tao, C. Zhang, J. Wang, W. Qiao, L. Ling, D. Long, Electrochim. Acta 188 (2016) 385–392.
[12] Z. Li, A. Ottmann, T. Zhang, Q. Sun, H.-P. Meyer, Y. Vaynzof, J. Xiang, R. Klingeler, J. Mater. Chem. 5 (2017) 3987–3994.
[13] H. Jiang, D. Ren, H. Wang, Y. Hu, S. Guo, H. Yuan, P. Hu, L. Zhang, C. Li, Adv. Mater. 27 (2015) 3687–3695.
[14] Y. Jing, Z. Zhou, C.R. Cabrera, Z. Chen, J. Phys. Chem. C 117 (2013) 25409–25413.
[15] M.V. Reddy, G.V. Subba Rao, B.V.R. Chowdari, Chem. Rev. 113 (2013) 5364–5457.
[16] W. Li, B. Zhang, R. Lin, S. Ho-Kimura, G. He, X. Zhou, J. Hu, I.P. Parkin, Adv. Funct. Mater. 28 (2018) 1705937.
[17] H. Sun, J.G. Wang, X. Zhang, C. Li, F. Liu, W. Zhu, W. Hua, Y. Li, M. Shao, ACS Sustain. Chem. Eng. 7 (2019) 5346–5354.
[18] K. Chang, D. Geng, X. Li, J. Yang, Y. Tang, M. Cai, R. Li, X. Sun, Adv. Energy Mater. 3 (2013) 839–844.
[19] Y. Chao, R. Jalili, Y. Ge, C. Wang, T. Zheng, K. Shu, G.G. Wallace, Adv. Funct. Mater. 27 (2017), 1700234.
[20] C. Zhu, X. Mu, P.A. van Aken, Y. Yu, J. Maier, Angew. Chem. Int. Ed. 53 (2014) 2152–2156.
[21] H.J. Chen, J. Huang, X.L. Lei, M.S. Wu, G. Liu, C.Y. Ouyang, B. Xu, Int J Electrochem. Sci. 8 (2013) 2196–2203.
[22] H. Wu, C. Hou, G. Shen, T. Liu, Y. Shao, R. Xiao, H. Wang, Nano Res. 11 (2018) 5866–5878.
[23] Y. Jiao, A. Mukhopadhyay, Y. Ma, L. Yang, A.M. Hafez, H. Zhu, Adv. Energy Mater. 8 (2018) 1702779.
[24] B. Lu, J. Liu, R. Hu, H. Wang, J. Liu, M. Zhu, Energy Storage Mater. 14 (2018) 118–128.
[25] L. Yang, S. Wang, J. Mao, J. Deng, Q. Gao, Y. Tang, O.G. Schmidt, Adv. Mater. 25 (2013) 1180–1184.
[26] Q. Zhang, Y. Cui, G. Qian, Coord. Chem. Rev. 378 (2019) 310–332.
[27] X. Han, H.G.W. Godfrey, L. Briggs, A.J. Davies, Y. Cheng, L.L. Daemen, A.M. Sheveleva, F. Tuna, E.J.L. McInnes, J. Sun, C. Drathen, M.W. George, A.J. Ramirez-Cuesta, K.M. Thomas, S. Yang, M. Schröder, Nat. Mater. 17 (2018) 691–696.
[28] J. Lee, C.Y. Chuah, J. Kim, Y. Kim, N. Ko, Y. Seo, K. Kim, T.H. Bae, E. Lee, Angew. Chem. 130 (2018) 7995–7999.
[29] X. Zhao, Y. Wang, D.-S. Li, X. Bu, P. Feng, Adv. Mater. 30 (2018) 1705189.
[30] G. Ferey, Science 309 (2005) 2040–2042.
[31] C. Rice, R.J. Young, R. Zan, U. Bangert, D. Wolverson, T. Georgiou, R. Jalil, K.S. Novoselov, Phys. Rev. B 87 (2013) 081307.
[32] H. Li, Q. Zhang, C.C.R. Yap, B.K. Tay, T.H.T. Edwin, A. Olivier, D. Baillargeat, Adv. Funct. Mater. 22 (2012) 1385–1390.
[33] B. Chakraborty, H.S.S.R. Matte, A.K. Sood, C.N.R. Rao, J. Raman Spectrosc. 44 (2013) 92–96.
[34] G. Xu, L. Yang, X. Wei, J. Ding, J. Zhong, P.K. Chu, Adv. Funct. Mater. 26 (2016) 3349–3358.
[35] Y.-L. Ding, P. Kopold, K. Hahn, P.A. van Aken, J. Maier, Y. Yu, Adv. Mater. 28 (2016) 7774–7782.
[36] J. Xiao, X. Wang, X.Q. Yang, S. Xun, G. Liu, P.K. Koech, J. Liu, J.P. Lemmon, Adv. Funct. Mater. 21 (2011) 2840–2846.
[37] F. Zhou, S. Xin, H.W. Liang, L.T. Song, S.H. Yu, Angew. Chem. Int. Ed. 53 (2014) 11552–11556.
[38] G. Wang, J. Zhang, S. Yang, F. Wang, X. Zhuang, K. Müllen, X. Feng, Adv. Energy Mater. 8 (2018) 1702254.
[39] C. Chen, X. Xie, B. Anasori, A. Sarycheva, T. Makaryan, M. Zhao, P. Urbankowski, L. Miao, J. Jiang, Y. Gogotsi, Angew. Chem. Int. Ed. 57 (2018) 1846–1850.
[40] S. Xia, Y. Wang, Y. Liu, C. Wu, M. Wu, H. Zhang, Chem. Eng. J. 332 (2018) 431–439.
[41] Q. Zhang, C.Y. Tsai, L.J. Li, D.J. Liaw, Nat. Commun. 10 (2019).
[42] X.H. Rui, N. Yesibolati, S.R. Li, C.C. Yuan, C.H. Chen, Solid State Ionics 187 (2011) 58–63.
[43] J. Deng, W.-B. Luo, X. Lu, Q. Yao, Z. Wang, H.-K. Liu, H. Zhou, S.-X. Dou, Adv. Energy Mater. 8 (2018), 1701610.
[44] Q. Liu, X. Su, D. Lei, Y. Qin, J. Wen, F. Guo, Y.A. Wu, Y. Rong, R. Kou, X. Xiao, F. Aguesse, J. Bareño, Y. Ren, W. Lu, Y. Li, Nat. Energy 3 (2018) 936–943.
[45] K. Xie, K. Yuan, X. Li, W. Lu, C. Shen, C. Liang, R. Vajtai, P. Ajayan, B. Wei, Small 13 (2017), 1701471.
[46] B. Jia, Q. Yu, Y. Zhao, M. Qin, W. Wang, Z. Liu, C.Y. Lao, Y. Liu, H. Wu, Z. Zhang, X. Qu, Adv. Funct. Mater. 28 (2018), 1803409.
[47] N. Zheng, G. Jiang, X. Chen, J. Mao, Y. Zhou, Y. Li, J. Mater. Chem. 7 (2019) 9305–9315.
[48] B. Jia, Y. Zhao, M. Qin, W. Wang, Z. Liu, C.Y. Lao, Q. Yu, Y. Liu, H. Wu, Z. Zhang, X. Qu, J. Mater. Chem. 6 (2018) 11147–11153.
[49] L. Xing, Q. Yu, B. Jiang, J. Chu, C.Y. Lao, M. Wang, K. Han, Z. Liu, Y. Bao, W. Alex Wang, J. Mater. Chem. 7 (2019) 5760–5768.